Science Advances
AAAS

advances.sciencemag.org/cgi/content/full/4/12/eaat9658/DC1

Supplementary Materials for

Glacial changes in tropical climate amplified by the Indian Ocean

Pedro N. DiNezio*, Jessica E. Tierney, Bette L. Otto-Bliesner, Axel Timmermann, Tripti Bhattacharya, Nan Rosenbloom, Esther Brady

*Corresponding author. Email: pdn@ig.utexas.edu

Published 12 December 2018, *Sci. Adv.* **4**, eaat9658 (2018)
DOI: 10.1126/sciadv.aat9658

This PDF file includes:

Section S1. Hydroclimate synthesis
Section S2. SST synthesis
Section S3. Climate model
Section S4. Simulations
Section S5. Initialization and climate equilibration
Section S6. Quantitative proxy-model agreement
Section S7. Climate response to ice sheet boundary conditions
Fig. S1. Climate response to exposure of the Sahul shelf as a function of land surface properties.
Fig. S2. Simulated patterns of hydroclimate change at the LGM.
Fig. S3. Proxy-model agreement for patterns of warm pool hydroclimate change at the LGM.
Fig. S4. Simulated patterns of IO cooling during the LGM.
Fig. S5. Impact of $U^{K'}_{37}$ and Mg/Ca-$\delta^{18}O$ calibrations on proxy-model agreement.
Fig. S6. Simulated rainfall response to LGM ice sheets.
Fig. S7. Simulated surface temperature response to LGM ice sheets.
Fig. S8. Simulated boreal summer response to LGM ice sheets.
Fig. S9. Boreal summer response to ice sheet albedo as a function of ocean-atmosphere coupling.
Fig. S10. Surface energy changes in response to ice sheet albedo as a function of ocean-atmosphere coupling.
Table S1. Updates to the synthesis of LGM hydroclimate.
Table S2. Compilation of SST proxies.
Table S3. Sea level simulations.
Table S4. LGM and single-forcing simulations.
References (*39*–*127*)

Section S1. Hydroclimate synthesis

We evaluate our simulations against a synthesis of hydroclimate changes at the Last Glacial Maximum (LGM) derived from rainfall-sensitive proxies. The current synthesis is an update to our previous compilation (*10*) incorporating new records published since year 2013, as well as corrections to existing records. A total of nine new sites were added to the synthesis (listed in Table S1). Proxy records from these sites largely agree with our existing synthesis suggesting drier LGM conditions relative to present over a large area of the Indo-Pacific warm pool (IPWP), from central Sulawesi (*3,39–41*), Flores and Sumba (*42,43*), to northern Australia (*44*). The one exception is a vegetation record from Northeast Borneo showing unchanged conditions (*43*), albeit not altering the overwhelming evidence that Borneo was also drier during the LGM. If interpreted in the context of the amount effect, proxy records tracking the isotopic composition of rainfall from Sulawesi and Sumatra (*40, 45*) suggest muted aridity or even wetter conditions during the LGM relative to present, in conflict with the overwhelming evidence for drier conditions, particularly in Sulawesi (*40*). In fact, Konecky et al. (*40*) argue that precipitation isotopes in these regions record shifts in moisture source, as opposed to the local amount of rain. Therefore, we exclude any isotopic records from this region when the inferred hydrological changes are not supported by other co-located proxy records.

A new record from inland East Africa (*46*) supports previous evidence of drier conditions over this region during the LGM. A new multi-proxy biomarker study shows reduced relative humidity over the eastern slopes of Mt. Kilimanjaro in Kenya (*47*). We exclude this record from our synthesis because relative humidity changes are not necessarily correlated with rainfall changes during LGM due to the effect of a globally colder climate. Riverine runoff records are also excluded from the synthesis due to complexities in their interpretation due to altered coastlines during the LGM, particularly over shallow marginal seas (*48*). Many of these records,

however, show changes consistent with the existing synthesis, supporting drier conditions over the IPWP center [e.g. (*49, 50*)] and unchanged conditions in the western Pacific [e.g. (*51*)]. Last, a lake level record from Lake Abhe was originally inferred to have been high during the LGM (*52*), but recent re-assessment of the record indicates that the lake was dry from 20,200 and 19,000 years BP (*53*). Therefore we categorize the site as dry during the LGM.

Section S2. SST synthesis

To facilitate the diagnosis of the mechanisms of LGM hydroclimate change, we compiled publicly-available sea-surface temperature proxy data from the Indo-Pacific Warm Pool (IPWP) region. These data must contain, at the least, LGM (19–23 ka) and Late Holocene (0–4 ka) data, and be located between 25°S – 20°N, 25 – 170°E, in order to match the spatiotemporal domain used in our previous hydroclimate and sea-surface salinity (SSS) categorical syntheses (*10*). Due to issues surrounding no-analog conditions in tropical microfossil assemblages (*54*) and difficulty in propagating errors for the assemblage multiple regressions, we focus on geochemical indicators for sea-surface temperature (SST): alkenone ($U^{K'}_{37}$) data ($n = 40$), paired Mg/Ca-δ^{18}O data ($n = 40$), and TEX_{86} data ($n = 5$). These data were previously compiled in ref. (*55*).

For the TEX_{86} data, we used the latest BAYSPAR SST calibration of ref. (*56*) and a prior standard deviation of 10°C to convert values to SST estimates. We did not apply older calibrations as these suffer from regression dilution and will yield an incorrect magnitude of change in warm tropical waters (cf. ref (*57*)). We applied several different calibrations to the alkenone and Mg/Ca data to test the sensitivity of our pattern correlations to calibration choice (results are described in Section 5 below). For $U^{K'}_{37}$ these included the Sonzogni '97 (*58*), and Muller '98 (*59*) calibrations as well as the new Bayesian calibration, BAYSPLINE (*55*), with both a generous 10°C and more informative 5°C prior standard deviation. For the Mg/Ca data, we corrected all data for dissolution and cleaning protocol differences in a consistent way prior

to applying calibrations: data were corrected by $11 \pm .049\%$ (2σ) if the authors of the original study used a reductive cleaning protocol (*60*) and by 0.054 ± 0.019 mmol mol^{-1} per μmol kg^{-1} ΔCO_3^{2-} (2σ) if the ΔCO_3^{2-} value (CO_3^{2-}-CO_{3sat}^{2-}) for the core site was below a threshold of 21.3 $\pm$ 6.6 (2σ) (*61*). This correction was done in a Monte Carlo fashion to propagate uncertainties.

The Mg/Ca calibrations applied included the Anand '03 multispecies sediment trap calibration (*62*), the Tierney '16 multivariate culture-based calibration (*37*), and the Gray '18 multivariate sediment trap calibration (*63*). The Anand '03 calibration assumes that Mg/Ca is only sensitive to temperature. The Tierney '16 calibration assumes that Mg/Ca responds to changes in both temperature and salinity. To solve for temperature, salinity must be estimated from paired $\delta^{18}O$ (sensitive to temperature and $\delta^{18}O_{seawater}$) and an assumption concerning the $\delta^{18}O_{seawater}$-SSS slope; for this we use the modern observed "all-tropics" $\delta^{18}O$-SSS slope (0.16) and intercept (-5.11) of Holloway et al., 2016 (*64*). This approach assumes that the $\delta^{18}O$-SSS relationship is stationary in time, which is a reasonable assumption in this case given that isotope-enabled modeling of the LGM found that the slope and intercept do not change substantially in the IPWP domain (*64*). The Gray '18 calibration assumes that Mg/Ca is sensitive to temperature, salinity, and pH. To solve for temperature, we once again used paired $\delta^{18}O$ data and also make an assumption about a glacial change in pH. Here, we follow ref. (*63*) and assume a whole-ocean increase in pH of 0.13 during the LGM.

In addition to the calibration treatments, for sites that used ^{14}C dates to constrain depth-age relationships, age models were calibrated to the Marine13 radiocarbon curve (*65*) for consistency. The LGM temperature anomaly is calculated as the difference between the mean of values between 19–23 ka and 0–4 ka. Table S2 lists all the core sites in the compilation, along with their location, data type, average LGM anomaly, and relevant references.

Section S3. Climate model

CESM1 consists of coupled general circulation models of the atmosphere and ocean, as well as sea ice and land models. Other components of the Earth system, such as the carbon cycle and marine ecosystems, can also be simulated using CESM1, however we kept them inactive because we focus here on the climate response to glacial boundary conditions. The atmospheric general circulation model is the Community Atmosphere Model Version 5 (CAM5) configured on a finite volume (FV) grid at a nominal horizontal resolution of 2° with 30 pressure levels for the vertical coordinate. CAM5 includes comprehensive parametrizations for the simulation of moist turbulence, a shallow and deep convection, cloud microphysics, and aerosol–cloud–rainfall interactions (*66*). The land model is the Community Land Model Version 4 (CLM4) configured on the same $2^\circ \times 2^\circ$ horizontal grid as the atmosphere model. CLM4 includes a prognostic carbon-nitrogen model, an urban canyon model, a prognostic land cover and land use, a crop model, a revised snow model with aerosol deposition of black carbon and dust, grain-size dependent snow aging, and vertically resolved snowpack heating (*67*). None of these features were active in our simulations with the exception of CLM's ability to pass dust mobilized by wind to the prognostic atmospheric aerosol module. This process is relevant for our study because dust emissions from exposed continental shelves could have an impact on rainfall by increasing aerosol loadings. The ocean general circulation model is the Parallel Ocean Program Version 2 (POP2) configured at the nominal horizontal resolution of 1°, with increased meridional resolution of about 1/3° on the equatorial wave guide, and 60 vertical levels. POP2 includes parameterizations for overflows, tidal mixing, and eddy mixing as described by (*68*). The reader is referred to a special collection of *Journal of Climate* (http://journals.ametsoc.org/page/CCSM4/CESM1) for a description of standard climate simulations performed with CESM1.

Section S4. Simulations

4.1. Pre-industrial control

Our control simulation was performed under pre-industrial boundary conditions, hereafter PI control. Greenhouse gas (GHG) concentrations were prescribed following the PMIP3 experimental protocol (`https://wiki.lsce.ipsl.fr/pmip3/doku.php/pmip3:design:pi:final`) using values of 280 ppm for CO_2, 760 ppb for CH_4, and 270 ppb for NO_2. Chlorofluorocarbon (CFC) concentrations were set to zero. Dust and other aerosol emissions were also set to pre-industrial values corresponding to year 1850. Ozone concentrations were prescribed using CAM5's default values. The solar flux was kept constant at 1365 Wm^{-2}. Land surface cover, including vegetation, glaciers, lakes, wetlands, and bare soil, follow CLM's default distribution for year 1850. This includes crops over India and China where large-scale agriculture was practiced by ancient civilizations. The orbital parameters were set to year 1850 AD. Note that the control simulation may still include some negligible anthropogenic influence due to the effect of pre-industrial agriculture on land surface properties.

4.2. Last Glacial Maximum

The 21ka boundary conditions were implemented as follows:

Greenhouse gases – Concentrations of long-lived GHGs were prescribed following the PMIP3 experimental protocol (`https://wiki.lsce.ipsl.fr/pmip3/doku.php/pmip3:design:21k:final`), with values of 185 ppm for CO_2 350 ppb for CH_4 and 200 ppb for NO_2. CFCs were set to 0, and Ozone concentrations were kept at pre-industrial values.

Orbital – The latitudinal and seasonal distribution of incoming solar radiation is calculated using CAM5's standard algorithm (*69*) with orbital parameters for the 21 ka BP interval. The solar flux was kept unchanged using the same value as in the control.

Ice sheets – Ice sheet topography and land surface glacier extent were prescribed following the PMIP3 protocol (`https://wiki.lsce.ipsl.fr/pmip3/doku.php/pmip3:design:21k:final`), which combined three different ice sheet reconstructions: ICE-6G v2.0 (*70–75*), GLAC-1 (*76, 77*), and the 2009 version of the ANU ice model (*78–80*). This blended reconstruction provides the ice sheet extent, land surface elevation, and land-sea mask for the Laurentide, Fennoscandian, Patagonian, and Anctartic ice sheets at the 21 ka BP interval. We included prescribed ice shelves over the western Labrador Sea following (*81*) to help alleviate stability problems associated with very steep topography gradients in this region. The final LGM ice sheet topography was computed by adding the difference between the reconstructed LGM minus the PI surface elevation to CAM5's standard topography as specified by the PMIP protocol. An additional 120 m were added globally to the CAM5 topography to represent the effect of lowered sea level.

Sea level / shelf exposure – The land-sea mask was modified in both CAM5 and CLM4 in order to represent the exposure of continental shelves during the LGM. The PMIP3 blended land-sea mask was used globally, with the exception of the Maritime Continent (MC), defined by the box 30°S–30°N, 90°E–160°E, where the land-sea mask was defined following (*12*).

Sea level / bathymetry and ocean passages – The bathymetry of POP2 was also modified following the PMIP3 experimental protocol resulting in the closure of several key passages, such as the Bering Straits. The bathymetry around the Maritime Continent was further modified following (*12*) with the objective of representing the effect of lower sea level on the Indonesian Throughflow (ITF). Lowering sea level by about 120 m results in the following changes: 1) blocked flow between the South China Sea (SCS) and the Indonesian Seas through Karimata straits (modern sill depth of 50 m), 2) no flow through the Java Straits due to Sunda exposure, and 3) a 120 m shoaling of the sill of the Makas-

sar, Lombok, Mindoro, and Sibutu passages (modern sill depths of 670 m, 220 m, 360 m, and 280 m respectively). Raising the sills of these passages leads to a slower thermocline flow, which is compensated by faster surface flow, resulting in small changes in depth-integrated transport (*12*).

Sea level / tidal mixing – The effect of altered tidal mixing due to exposed shelves was implemented following the approach of (*12, 82*), resulting in increased mixing over the Banda Sea and decreased mixing off the exposed Northwestern Australian Shelf.

Mean ocean salinity – The effect of reduced ocean volume on salinity was represented by adding 1 psu to the ocean initial conditions. This effect was already included in the initial conditions obtained from an existing LGM simulation performed with the Community Climate System Model Version 4 (CCSM4), the predecessor of CESM1. More details on initialization are given in section 5.

Vegetation – Vegetation was prescribed to be the same as in the control simulation, except for the regions covered by ice sheets or exposed due to lowered sea level. Different plant functional types (PFTs) were prescribed over exposed shelves according to the latitude. C_3 Arctic grass PFT was applied over shelves poleward from 60°. C_3 grass PFT was applied over shelves poleward from 30°. An equal mix of tropical deciduous tree and C_4 tropical grass was prescribed over tropical shelves (equatorward from 30°), including the Sunda and Sahul shelves (*12*). This setup is based on evidence that the Sunda Shelf was a savanna (i.e. mainly tropical grass) environment during the LGM (*83*). (*12*) explored the sensitivity to other PFTs such as C_3 grass, bare soil, and tropical forest and did not find substantial changes, indicating that the results are not sensitive to the vegetation cover. The remaining surface properties, such as albedo or surface roughness, are computed by CLM4 based on the soil and plant properties and passed to CAM5 model via the coupler. The vegetation phenology, including the total leaf and stem area indices and

canopy heights, are prescribed and do not respond to changes in climate.

Runoff – Runoff over exposed shelves and snow accumulation over the ice sheets were redirected to the nearest ocean grid point in order to maintain a balanced freshwater budget. Routing of snow accumulation mimics iceberg discharge; however, these fresh water fluxes do not have the magnitude to represent the iceberg discharge associated with Heinrich events. Therefore the climate response to these abrupt events is not simulated.

Overflows – Parametrized overflows in the Ross and Weddell Seas were removed in all simulations with ice sheets because the associated ice shelves extend over the overflow source regions. The Denmark Strait and Iceland/Scotland overflows were kept unchanged as in the control simulation. The number of bottom levels was increased from 2 to 6 in order to alleviate an advective instability (*81*).

Dust – CAM5 was configured to run with its prognostic aerosol module requiring prescribed aerosols and dust emissions. All our simulations were run with the same dust emissions as in the control. There is evidence that high latitude dust deposition rates were from 2 to 20 times larger during glacial periods than interglacial periods (*84–87*). The increased dust loadings appear to be restricted to high latitudes (*84–86*), with little direct impact on the tropics (*88*). Dust-driven cooling of high latitudes could still drive inter-hemispheric temperature gradients that can alter patterns of tropical rainfall (*29*). These processes, however, are likely to be of second order relative to the magnitude of Northern Hemisphere cooling caused directly by the higher albedo of ice sheets.

4.3. Single forcing simulations

The single forcing simulations are listed in Table S4. Additional simulations isolating the effect of exposure of the Sunda and Sahul shelves are listed in Table S3. The procedure followed to isolate each climate response is described in Table 1 of the main manuscript.

4.3.1. Icesheets

We performed a series of simulations exploring different aspects of the response to ice sheets. Simulation LGM_{ICE} includes all the ice sheet boundary conditions described in section 4.2, with the remaining glacial forcings (GHGs, orbit, sea level) set to preindustrial values. These simulations include a 120 m increase in continental height due to lowered sea level, but no altered coastlines. Differencing the climate of LGM_{ICE} minus PI allows us to isolate the full climate response to ice sheets. Additional simulations were performed with the objective of isolating the response to ice sheet topography from the response to ice sheet albedo. Simulation LGM_{TOPO} included the topography of the ice sheets (and the 120 m increase in continental height), but with land surface properties defined as as in the control. In this simulation, the "brown" ice sheets exert mechanical forcing to the atmosphere, potentially affecting the atmospheric circulation, however without the cooling effect of the higher albedo. This simulation shows -1.05 K of surface cooling over the tropics (30°S–30°N), which cannot be entirely explained by the 120 m increase in continental height – the "lapse rate" effect in agreement with similar simulations (*89*). The elevation of the Laurentide and Fennoscandian ice sheets represents an additional cooling factor (fig. S7b). The Sahel, Arabia, and India, also show pronounced cooling (fig. S7b) potentially linked to increased monsoonal rainfall (fig. S6b) via changes in cloud cover. Differencing the climate of LGM_{TOPO} minus PI allows us to isolate the climate response to ice sheet topography (shown in figs. S6c, S7c, and S8c).

The response to albedo can be computed via two methods. The first method isolates the effect of albedo relative to the LGM topography. This response is obtained differencing the climate of LGM_{ICE} from LGM_{TOPO}. Both simulations have ice sheet topography set to LGM values, but differ in the surface properties over the areas covered by the Laurentide, Fennoscandian, and Patagonian ice sheets. This approach isolates the cooling effect of ice sheet albedo at

high altitude. The rainfall and surface temperature changes isolated via this method are shown in figs. S6c, S7c, and S8c. The second method isolates the effect of albedo relative to the control topography. To estimate this response we ran an additional simulation with the distribution of continental ice set at LGM values, but over the modern topography. The response to albedo can also be estimated by differencing the climate of this LGM_{ALB} simulation from the PI control. This approach isolates the cooling effect of the albedo of the ice sheets relative to the modern topography. The rainfall and surface temperature changes isolated via this method are shown in fig. S6d and S7d. We discuss the differences between the responses obtained from these two approaches in section 7.

4.3.2. Sea level

An additional set of simulations were run focused solely on the effect of sea level on the geography and bathymetry of the Maritime Continent. In these simulations we applied the "Sea level" boundary conditions described in section 4.2 over the MC box. Outside this region all boundary conditions were set at PI values. These simulations were extensively analyzed in a previous study showing the importance of coupled air-sea interactions in the climate response to exposure of Sahul shelf (*12*). Simulations LGM_{SUNDA}, LGM_{SAHUL}, and $LGM_{SUNDA+SAHUL}$ include the effect of exposure of the Sunda, Sahul, and both shelves combined respectively. These simulations allowed us to isolate the role of each shelf in the full response. The LGM_{SL} simulation includes exposure of both shelves plus additional effects of lower LGM sea level over the Maritime Continent region, such as shallower ITF passages and increased tidal mixing. These additional factors drive negligible changes compared to shelf exposure (*12*).

Dependence on shelf surface properties

Our standard setup consists of Sunda and Sahul shelves covered with an equal mix of tropical deciduous tree and tropical grass (C_4) plant functional types (PFTs) (see section 4.2, veg-

etation). This setup is based on paleoenvironmental evidence suggesting that the *Sunda* shelf was a savanna environment, i.e. mainly tropical grass, during the LGM (*83*). However, the paleoenvironmental evidence is less conclusive for the *Sahul* shelf, since some studies suggest an estuarine environment over the Gulf of Carpentaria (*90, 91*). We addressed this issue with additional simulations configured with other PFTs, particularly a case where the Sahul shelf is covered by wetlands to mimic an estuarine environment. The simulations show that surface cover by wetlands, 100% C_4 grass, or bare soil, do not show substantial difference in the rainfall and SST changes over the Indian Ocean (fig. S1). The only differences are located off the coast of northern Australia, where the model simulates pronounced coastal warming in the vegetated and bare soil cases (figs. S1c, S1e, and S1g). This response is caused by warming of the adjacent Sahul shelf during austral Spring due to a reduction in evaporative cooling because the land surface is drier than in the wetland case (*12*). All simulations show consistent large-scale changes over the Indian Ocean regardless of the surface properties showing this coastal warming is not essential for the large-scale response. Instead, the large-scale response is controlled by the albedo of the shelf surface (*12*), which increases in all cases, including the wetland case.

4.3.3. Greenhouse gases

We performed an additional simulation in which GHG concentrations are set to LGM values and all other boundary conditions are kept unchanged as in the PI control. This simulation (LGM_{GHG}) allows us to estimate the climate response to lower LGM GHG concentrations. An ddditional simulation was run combining all sea level boundary conditions over the MC box (LGM_{SL}) with LGM GHGs and orbit ($LGM_{SL+GHG+ORB}$).

Section S5. Initialization and climate equilibration

Our LGM simulation was run until the climate system, including the deep ocean, was close to radiative equilibrium. This simulation was initialized from a similar LGM run performed with version 4 of the Community Climate System Model (CCSM4), which was also run to near equilibration (*81*). As a result our simulation required only 500 years for the ocean to reach a new equilibrium with the LGM forcings. We ran the model for an additional 600 years to obtain a sufficiently stable and long climate to compute climatologies. During this period the deep ocean continues to adjust to the forcing, however at slower rates ranging from 0.1 K per century near the surface m and less than 0.05 K per century below 2000 m (not shown). The north Atlantic shows the largest trends, which can reach to 0.15 K per century in areas of deep convection down to 2000 m. Our full ice sheet only simulation, LGM_{ICE}, was initialized from the last year (year 1100) of the new LGM simulation. Because this simulation has PI GHG forcing it took 700 years to warm up until the climate equilibrated. The last year of this simulation was used to initialize the other ice sheet simulations, which required a shorter equilibration time of about 100 years. Our GHG simulation (LGM_{GHG}) was initialized from the last year of an existing simulation with LGM GHGs (*81*). All of our sea level simulations were initialized from the PI control. Our simulation combining sea level, GHGs, and orbit, LGM_{SL}GhgOrb, was initialized from LGM_{SL} and took 300 years to cool down and equilibrate.

Section S6. Quantitative proxy-model agreement

The role of each glacial forcing and associated mechanisms was assessed by quantifying the agreement between the simulated changes with two multi-proxy reconstructions.

6.1. Hydroclimate

We explored the sensitivity of the proxy-model agreement to the spatial extent of the proxy network by computing Cohen's κ values over four subdomains dominated by different responses. Over East Africa and India (25–80°E 25°S–20°N), the highest $kappa$ values are for the "SL_{MC} + GHG + orbit" and "SL_{MC} + IS_{albedo}" responses (fig. S3c). This part of the network captures the dipole of dry/wet inland/coastal Africa driven by GHGs and sea level, as well as the drying over India and the Horn of Africa driven by ice sheet albedo. In contrast, the proxies over warm pool center (80–145°E 25°S-20°N) show significant ($p < 0.33$) κ values for sea level response because these proxies are well distributed to capture the associated drying pattern (fig S3d). The proxies located north of the equator do not show statistically significant κ values for any responses (fig. S3e). The proxies located south of the equator, in contrast, show the largest κ values for responses to altered sea level boundary conditions (fig. S3f). This part of the proxy network is better suited to capture the dipole of dry warm pool and wetter east Africa, which is more pronounced south of the equator. This analysis indicates that the proxy network is well suited to capture all the responses simulated by our model. The response to ice sheet albedo cannot be isolated with statistical significance. However, it improves the agreement in combination with the sea level response (Fig. 4, fig. S3b).

6.2. Sea-surface temperature

We also assessed the agreement between simulated SST changes (fig. S5) and reconstructions of LGM temperature changes derived from sedimentary $U_{37}^{K'}$, Mg/Ca-δ^{18}O, and TEX_{86} data. These reconstructions are quantitative, therefore we estimate agreement by calculating the pattern correlation between proxy-estimated and model-simulated values at the core sites. We applied different temperature calibrations to the $U_{37}^{K'}$ and Mg/Ca data as described above in Section 2 to explore the sensitivity of the model-proxy agreement to calibration choice. The three

Mg/Ca estimates combined with the four $U_{37}^{K'}$ estimates resulted in an ensemble of twelve different SST change reconstructions. For each of these reconstructions, we computed the pattern correlation with the simulated SST changes at the proxy sites over the 30°E–110°E 25°S–25°N domain. This region excludes the region off the coast of the Sahul shelf where simulated SST changes are highly sensitive to the land surface properties, but have little impact on the large-scale response (see Section 4.3.3 for further details). The model-proxy agreement is largely independent of the calibrations used to estimate the SST changes (fig. S5). Most calibrations show the highest significant correlations with the simulated SST changes in response to either full sea level boundary conditions or sea level plus ice sheet albedo. The reconstructions using the Anand '03 calibration for Mg/Ca show lower correlations and significance levels for the single-forcing experiments because the reconstructed cooling over the eastern IO is not as strong as in the model simulations (fig. S4d). Overall, this analysis demonstrates that our conclusions are not sensitive to the calibrations used to estimate SST changes.

Section S7. Climate response to ice sheet boundary conditions

Here we provide a more detailed discussion of the mechanisms involved in the response of the Indian Monsoon to ice sheet boundary conditions. We isolate the responses to albedo and topography, and explore whether these responses interact nonlinearly. Previous studies suggest that the response of the extra-tropical circulation to ice sheet topography and albedo (*89,92–94*). Less is known regarding nonlinearities in the tropical response. A recent study has shown that the temperature and rainfall responses to LGM GHGs and ice sheets are largely linear (*95*), particularly in the tropics. However, this study did not separate the responses to ice sheet albedo and topography. A previous study showed that albedo can have a larger effect on Pacific climate depending on the altitude of the ice sheets (*96*), but did not focus in the Indian monsoon. Here we revisit this issue computing the response to albedo, both relative to PI or LGM topography,

in order to exclude or include these interactions.

The annual-mean response to full ice sheet boundary conditions shows drying over the western IO, Arabian Sea, the Indian subcontinent, and over the South China Sea (fig. S6a). Analysis of the individual responses shows that albedo plays a more dominant role than topography in causing the patterns of drying over the IPWP warm pool, particularly the drying over India (fig. S6, bottom). The topography of the ice sheets causes wetter conditions in the region (fig. S6b). The two approaches to isolate the response to albedo yield responses with different rainfall patterns over the Pacific (fig. S6c vs. fig. S6d), revealing nonlinear interactions between albedo and topography. These nonlinearities could arise from changes in atmospheric circulation over the North Pacific, which previous studies showed can cause tropical cooling via intensification of the subtropical cell and equatorial upwelling (*97*). In contrast, the response over the Indian Ocean and monsoon domain exhibits similar responses for either method (fig. S6c vs. fig. S6d). This suggests a more linear response, and therefore, a lesser role for changes in extratropical circulation as in the Pacific. In the next subsection we discuss the mechanisms driving this changes by focusing on the summer time response.

7.1. Monsoon response

The most prominent feature of the ice sheet response over the Indian ocean is a weakening of the Indian Summer Monsoon (ISM), which is seen as a reduction in rainfall over the Arabian Sea and the Indian subcontinent during July-August-September season (Fig. 5 and fig. S8a). Ice sheet *topography* has an influence over this region, but the changes are opposite in sign of the full response (fig. S8b). Our simulations show that the glacial weakening of the ISM is driven by the effect of ice sheet *albedo* (figs. S8, bottom). The ISM drying is stronger in magnitude when computed relative to LGM topography (Fig. S8c) than relative to the control topography (fig. S8d). However, both methods yield similar large-scale patterns over Africa

and India suggesting that the main characteristics of the response are largely independent of ice sheet topography. In the following, we focus our analysis on the albedo response relative to LGM topography.

We performed an additional set of simulations with the objective of identifying the mechanisms involved in the ISM response to ice sheet albedo. These simulations were ran with CESM1 configured with the same atmosphere and land models (CAM5 and CLM4) coupled to ocean models of varying complexity. In all cases the response to albedo was isolated relative to LGM topography (LGM_{ICE} – LGM_{TOPO}). First we replaced the fully dynamical ocean (POP2) with a model of the ocean mixed layer. In this model, the effect of vertical mixing, entrainment, and horizontal currents is prescribed as a seasonally-varying heat source, or Q-flux. Because the effect of these ocean processes on SSTs is fixed, changes in sea-surface temperature (SSTs) computed by this "slab" ocean model can only be influenced by energy exchanges with the atmosphere, such as changes in evaporation or clouds. Note that this configuration uses CICE, the fully interactive sea ice model, as in the fully-coupled configuration. In the second case, the ocean model consists of climatological SSTs and sea ice extent from the pre-industrial (PI) control. In this configuration the air-sea heat fluxes are computed but cannot change the fixed SSTs and sea ice extent. Because SST and sea ice remain unchanged all climate changes simulated in this configuration are due to atmosphere changes *uncoupled* from the ocean, but influenced changes over land. For each "slab" and "SST-forced" configuration we ran a PI, LGM_{ICE}, and LGM_{TOPO} simulation for 100 years after 10 years of equilibration. All slab ocean simulations were run with Q-flux computed from the fully-coupled PI control and boundary conditions as in the corresponding fully-coupled case as specified in Table S4. Similarly, all SST-forced simulations were ran with seasonally-varying climatological SSTs and sea ice cover obtained from fully-coupled PI control and all other boundary conditions as in the fully-coupled cases as specified in Table S4. The resulting "thermally coupled" and

"uncoupled" responses were computed as in the fully-coupled case (LGM_{ICE} – LGM_{TOPO}).

Our hierarchy of simulations shows that most of the features of the boreal summer response simulated independently of the degree of ocean-atmosphere coupling (fig S9). All simulations show cooling over the Northern Hemisphere continents extending equatorward over Africa and Asia (fig S9a, fig S9b). We tested the relative roles of the Northern Hemisphere ice sheets with an additional simulation where continental ice was prescribed only over the Fennoscandian ice sheet (FIS). This simulation exhibits much weaker cooling relative to the response to both ice sheets combined (not shown), indicating that the Laurentide ice sheet (LIS) is the dominant driver of the changes. These results confirmed that the cold air generated by the lower albedo of the LIS is advected by the mid-latitude westerlies cooling the Northern Hemisphere continents. In addition, CESM1 simulates a zonal band of land surface *warming* extending from the Sahel to northern India. (fig. S9 top, red shading). Collocated with this band of warming, CESM1 simulates a band of reduced rainfall (fig. S9, middle) that extends along the edge of the Saharan and Arabian deserts. For timescales involved in the seasonal response of the monsoons to northern cooling, deep convection is expected to be controlled by the distribution of subcloud layer entropy (*98*). We diagnosed the changes in moist entropy in terms of the equivalent potential temperature, θ_e, using Bolton's formula (*99*). The subcloud-layer entropy is defined as θ_e values on a terrain-following model level about 20 hPa above the surface as in (*35*). We find that the band of reduced rainfall is also characterized by reduced sub cloud θ_e (fig. S9 bottom), indicative of an environment that is less conducive for deep convection.

Thermodynamic coupling with the ocean increases the magnitude of the land surface temperature and rainfall changes, but does not change their spatial pattern (fig. S9. This demonstrates the dominant role of atmospheric processes communicating high latitude albedo cooling to the northern hemisphere tropics. The response with a fully-coupled ocean is nearly identical to the slab-ocean configuration (not shown), therefore we focus our analysis on the "uncoupled"

and "thermally coupled" responses. We propose the following link between albedo cooling over the LIS and the the drying of the ISM. Colder and drier glacial air generated over the LIS is advected downstream by the climatological mid-latitude westerlies. This air is mixed equatorward by atmospheric eddies displacing warm and moist air during the summer advance of deep convection associated with the Afro-Asian monsoon. This response is consistent with the "ventilation" mechanism proposed as a limit for the poleward extent of the monsoons (*32*). A similar response was seen in simulations in response to North Atlantic cooling (*33*), which is consistent with our analysis since both regions of high latitude cooling are upstream from the monsoonal response. Feedbacks internal to the monsoons appear to further amplify their initial retraction. Our simulations show that the anomalous meridional gradient in land surface temperature (fig. S9 top, shading) drives an anomalous meridional circulation (fig. S9 top, vectors). These changes in circulation reinforce the initial weakening of the monsoon by enhancing the equatorward advection of cold and dry air.

The area with reductions in deep convection is accompanied by surface warming of about 2K (fig. S9 top, red shading). Our simulations indicate that this warming is a response to the reduction in convection and not a driver. Diagnosis of changes in surface energy fluxes changes shows that the warming over the Sahel, Arabian Peninsula, and south Asia is caused by a decrease in cloud cover (fig. S10a–c) and associated increased surface radiation (fig. S10d–f). This *increase* in surface radiation in cloudy skies is balanced by a *decrease* in surface radiation in clear skies (fig. S9g–i). This response is caused by decreased water vapor absorption as the air column becomes much drier when the monsoons retreat. A decrease in evaporative cooling also contributes to the surface warming (fig. S9j–l). These changes in surface energy fluxes are ultimately balanced by an increase in sensible heat flux (fig. S9m–o) and associated land surface warming (fig. S9a–d). Ice sheet topography drives a response that is largely the opposite to albedo, with muted cooling over the Saharan and central Asia, and cooling over the Sahel,

the Arabian peninsula, and India (fig. S10b), and increased monsoon rainfall (fig. S11b).

This analysis shows that the mechanisms linking albedo cooling with the retreat of the Afro-Asian monsoon do not involve changes in SSTs or ocean circulation. The sole exception is the core ISM region, where rainfall reductions are present in the thermally- and fully-coupled responses (Figs. 5b and 5c or S9d), but not in the uncoupled case (Fig. 5a or fig.S9c). Cooling over the Arabian sea plays a key role explaining the rainfall reductions over the ISM core region simulated in the thermally- (Figs. 5e or S9d) and fully-coupled cases (Fig. 5f). The colder SSTs reduce the convergence of moisture by the climatological monsoon driving a reduction in rainfall over the core ISM region. This thermodynamic reduction in moisture convergence overwhelms the dynamic effect of increased monsoonal flow, which otherwise would increase ISM rain, as seen in the uncoupled case (Fig. 5a or fig. S9c).

Further analysis of the uncoupled case shows that the cooling of the Arabian sea is initiated by the retreat of the Afro-Asian monsoon discussed above. This link is established as follows. The retreat of the Afro-Asian monsoon warms the Arabian Peninsula (Figs. 5d and S9a) creating a land-sea contrast relative to the Arabian sea, which remains unchanged. This gradient drives stronger along-shore winds via thermal wind balance (Fig 5d, vectors). The increased wind speed associated with these anomalous winds drive cooler SSTs via increased evaporative cooling, seen in as a negative change in latent *air-sea* heat flux over the Arabian Sea (fig S10j, blue shading). Thermodynamic coupling allows theses processes to influence SSTs, resulting in cooling of the Arabian sea (Figs. 5e and S9b). The fully coupled response (Figs. 5f) is slightly stronger to the thermally-coupled response (Figs. 5e), suggesting that changes in ocean currents or upwelling play a secondary role amplifying the cooling of the Arabian sea.

In summary, our hierarchy of simulations allowed us to identify mechanisms linking a weaker ISM at the LGM with Northern Hemisphere cooling. According to this mechanism, high-latitude albedo cooling has the largest effect on tropical climate in boreal summer. Cold

glacial air mixed into the tropics renders atmospheric conditions unfavorable for deep convection over Africa and Asia slowing down the seasonal advance of the monsoon systems. This monsoon "ventilation" communicates ice sheet albedo cooling through land-atmosphere processes across the Saharan and Arabian deserts, ultimately leading to enhanced glacial cooling of the Arabian sea and pronounced weakening of the Indian summer monsoon. This new mechanism more generally explains the link between monsoon weakening during other intervals characterized by Northern Hemisphere cooling, expanding on previous studies that previously linked weaker ISM to Arabian SST cooling (*36, 37*).

All the terrestrial records in our synthesis are consistent with rainfall reductions associated with a weaker ISM during LGM. Furthermore, there is growing evidence from remote isotopic records that the ISM weakened in response to glacial conditions over the past 120 ka (*100*), also supporting our conclusions. Our proposed mechanism is also well supported by the SST proxies, which show pronounced cooling over the Arabian Sea. The enhanced land warming, another key element of our mechanism, is, in contrast, more challenging to constrain. A record from northern Oman (*101*) is ideally located to capture this warming signal. This record shows ~ 6.5 K of cooling during the LGM. This value is not necessarily at odds with our simulations because the warming associated with enhanced monsoon ventilation is a summertime response and can be overwhelmed by cooling during winter time, resulting in a more muted cooling. This can be seen in our albedo-only simulations, which show annual mean cooling of about 2K over this region (fig. S7c). More importantly, while the albedo-only response shows muted annual mean warming over parts of North Africa and Arabia due to monsoon ventilation and winter cooling combined (fig. S7c), the additional effects of ice sheet topography drive additional annual mean cooling (fig. S7a). Including the cooling effect of lowered GHGs would lead to more pronounced cooling and closer agreement with the the northern Oman record (*101*).

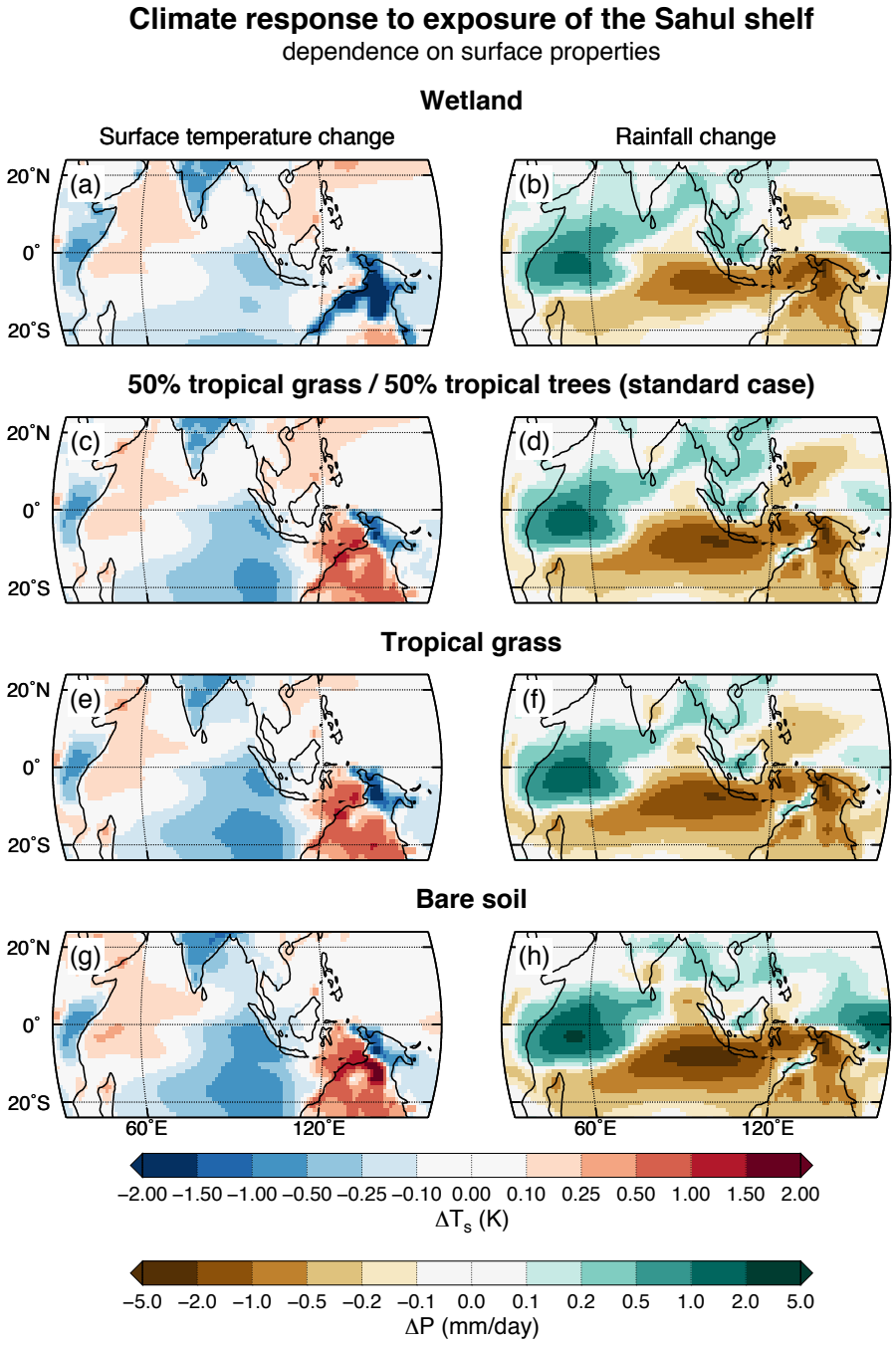

Fig. S1. Climate response to exposure of the Sahul shelf as a function of land surface properties. Changes in surface temperature (left) and rainfall (right) simulated by CESM1 in response to exposure of the Sahul shelf. Responses simulated for different types of land surface cover are shown.

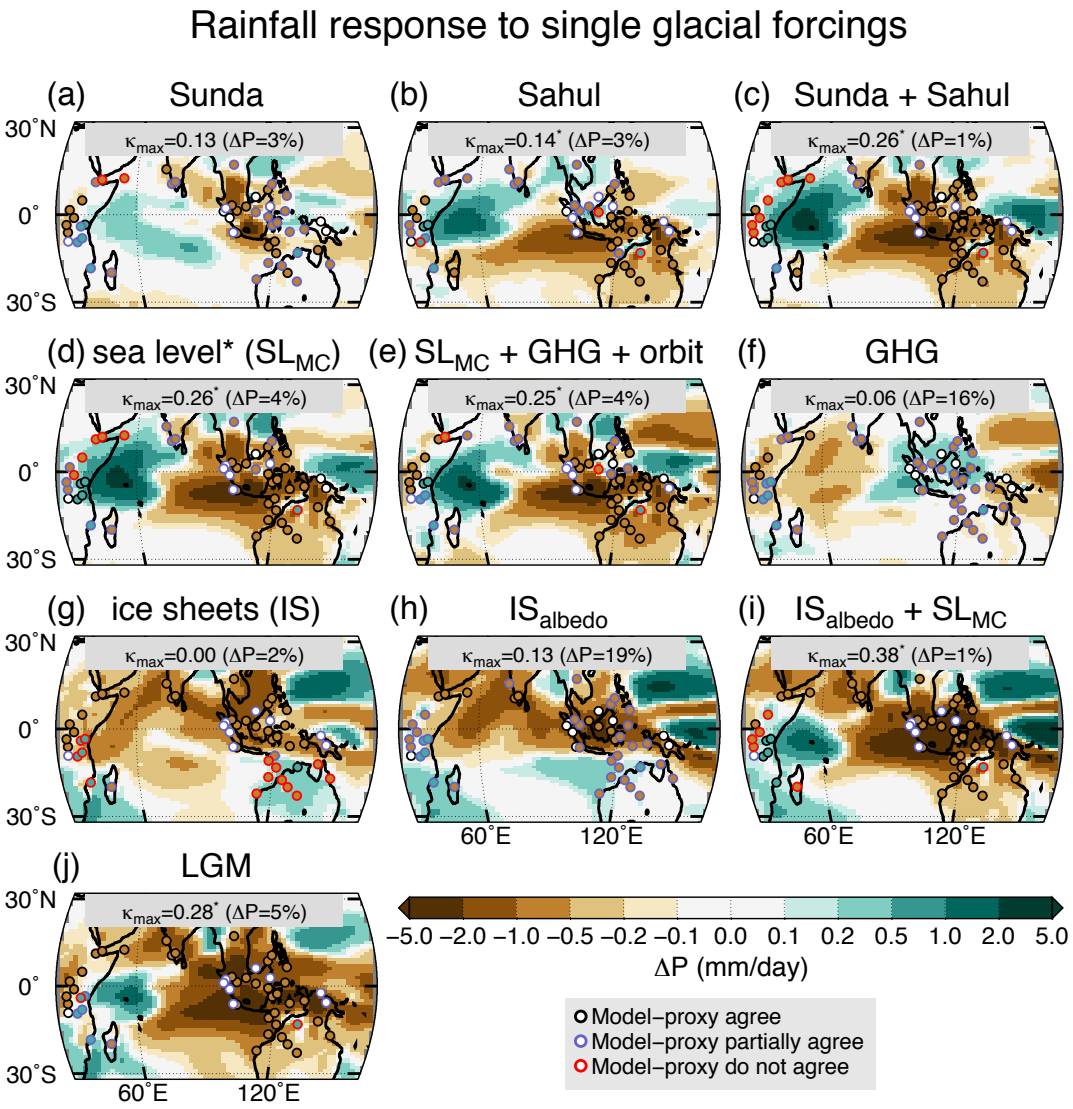

Fig. S2. Simulated patterns of hydroclimate change at the LGM. Rainfall changes simulated by CESM1 in response to individual glacial boundary conditions (shading). Proxy-inferred changes (circles) with outer color indicating the level of agreement with the simulated changes. The maximum Cohen's κ and optimal threshold for defining drier or wetter conditions is shown for each climate response. Asterisks indicate statistical significance ($p < 0.05$). The climate responses and associated boundary conditions are listed in Table 1 of the main manuscript.

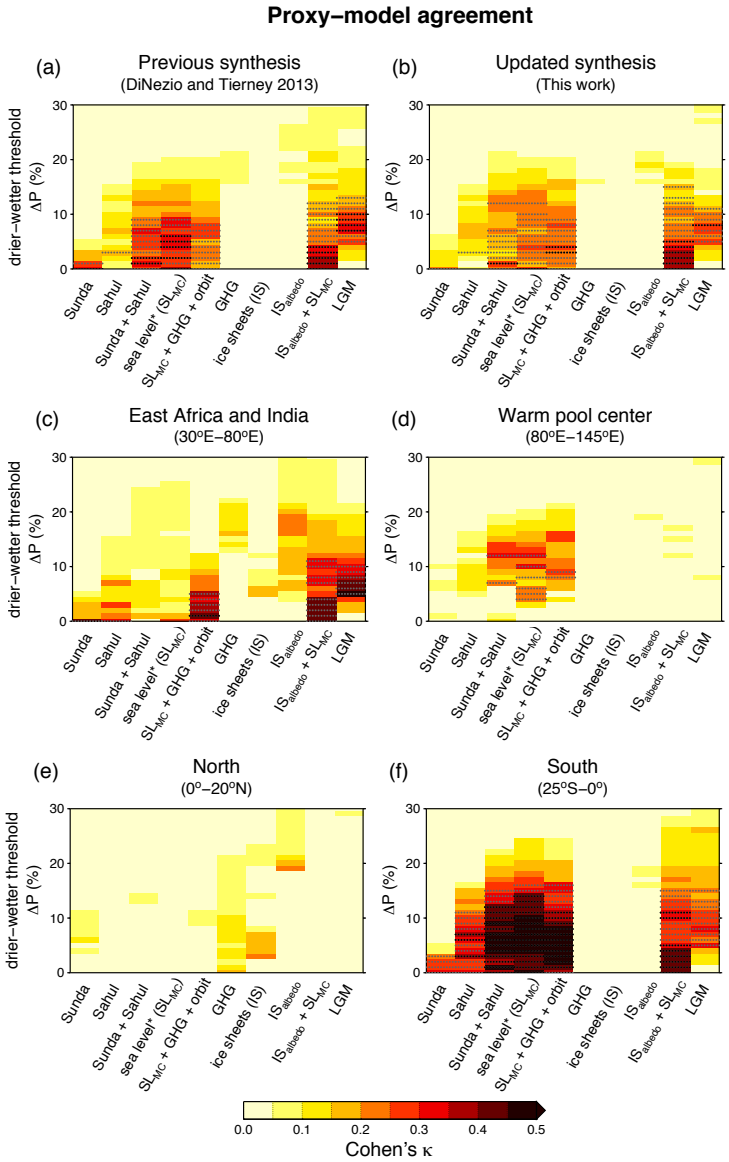

Fig. S3. Proxy-model agreement for patterns of warm pool hydroclimate change at the LGM. Cohen's κ between the simulated climate responses to different LGM boundary conditions (x-axis) and (a) our previous multi-proxy reconstruction (*10*) and (b) its updated version (this work). Cohen's κ derived from the updated reconstruction for the following subdomains: (c) East Africa and India (25°E–80°E 25°S–20°N), (d) the warm pool center (80°E–145°E 25°S–20°N), (e) the southern tropics (25°E–145°E 25°S–0°) and (f) northern tropics (25°E–145°E 0°–20°N). Panels c–f are based on the updated synthesis. The climate responses and associated boundary conditions are listed in Table 1 of the main manuscript. Cohen's κ values are given as a function of wetter/drier threshold (y-axis). Gray and black stippling indicate 1σ ($p < 0.33$) and 2σ ($p < 0.05$) statistical significance.

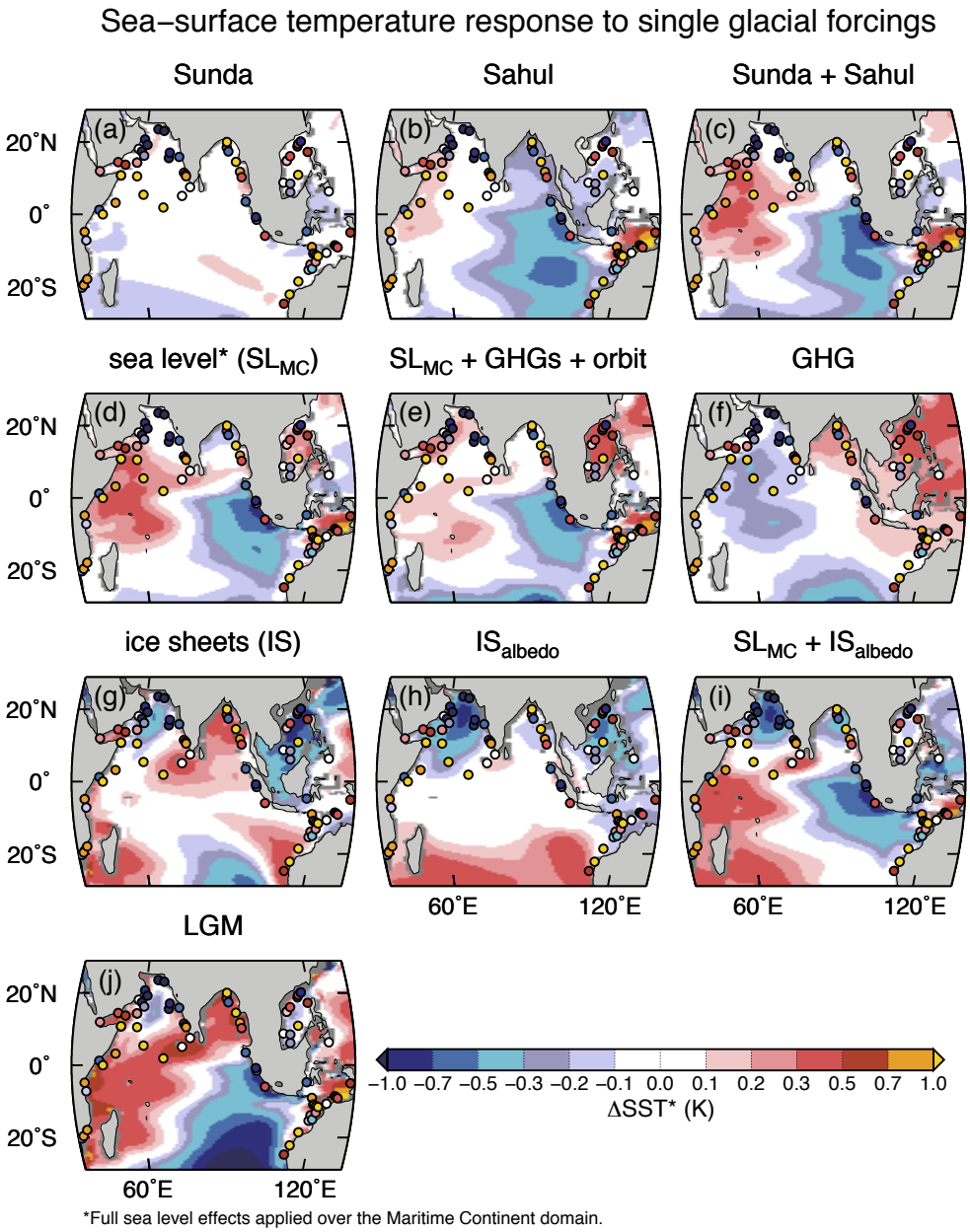

Fig. S4. Simulated patterns of IO cooling during the LGM. Sea-surface temperature changes simulated by CESM1 in response to individual glacial boundary conditions (shading). Overlaid circles show proxy-inferred changes in SST. The tropical mean (30°S-30°N) change is removed from both simulated and proxy-inferred changes in to order emphasize horizontal gradients. The climate responses and associated boundary conditions are listed in Table 1 of the main manuscript.

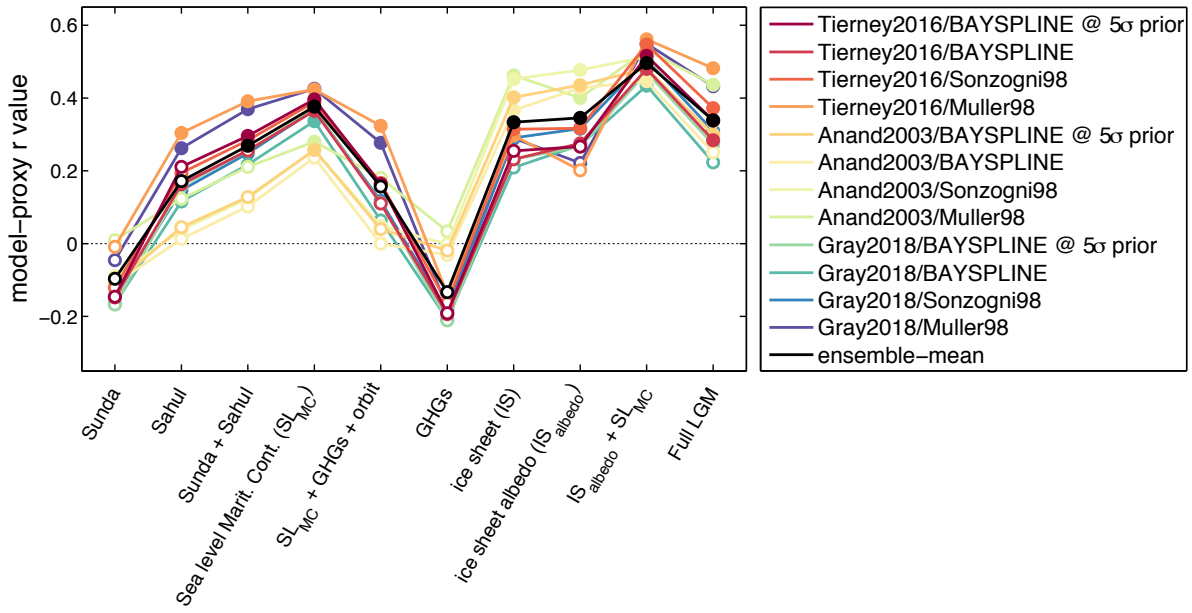

Fig. S5. Impact of $U_{37}^{K'}$ and Mg/Ca-$\delta^{18}O$ calibrations on proxy-model agreement. Pattern correlation coefficient (y-axis) between sea-surface temperature (SST) changes from single forcing simulations (listed in x-axis) and proxies. Color curves indicate correlation values computed using different SST calibrations for Mg/Ca-$\delta^{18}O$ and $U_{37}^{K'}$ measurements. The black curve indicates the correlation values between the simulated SST changes and the average from all calibrations (ensemble mean). Solid circles indicate statistical significance ($p < 0.05$). Proxy records from the 30°E–110°E 25°S–25°N region are used to compute the pattern correlation coefficient. This excludes the region off the coast of the Sahul shelf where simulated SST changes are highly sensitive to the land surface properties, but have little impact on the large-scale response (see Section 3.3.3 for further details).

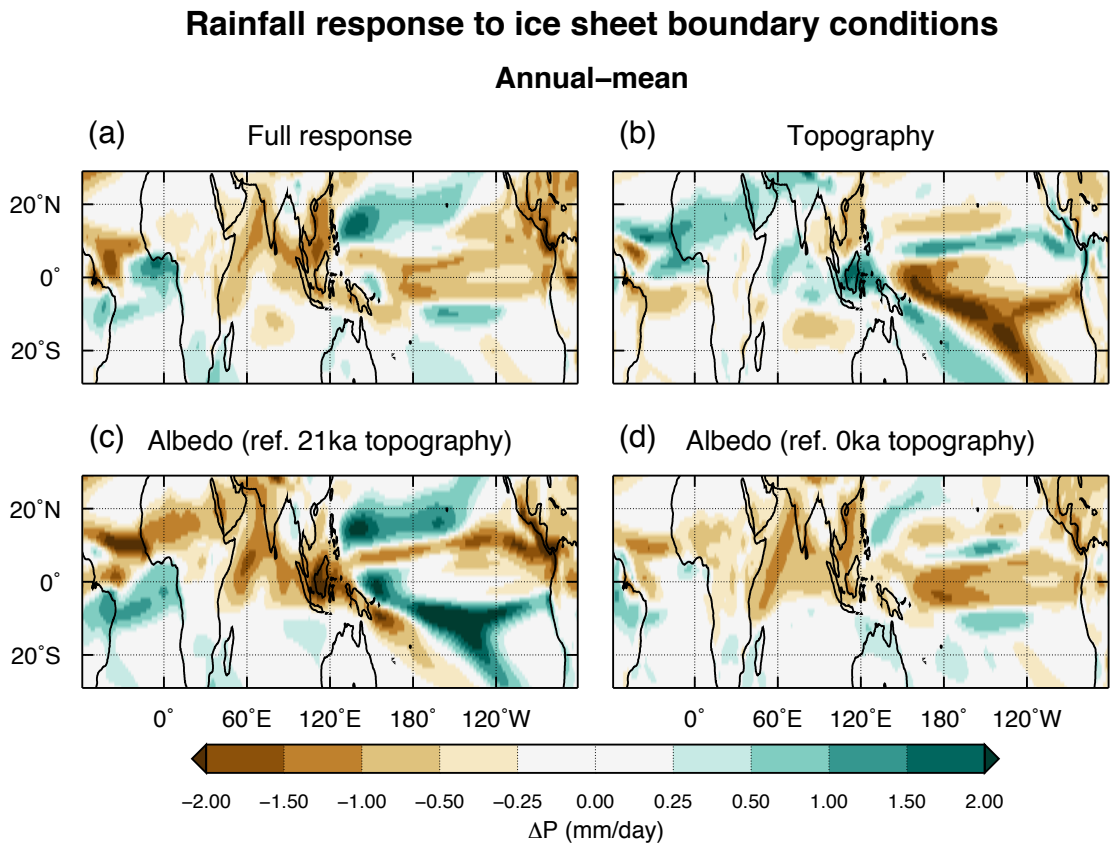

Fig. S6. Simulated rainfall response to LGM ice sheets. Annual-mean rainfall changes simulated by CESM1 in response to (a) full, (b) topography, and (c,d) albedo ice sheet boundary conditions. Refer to Table 1 for details on the computation of each climate response. Coastlines correspond to a 120 m drop in sea level.

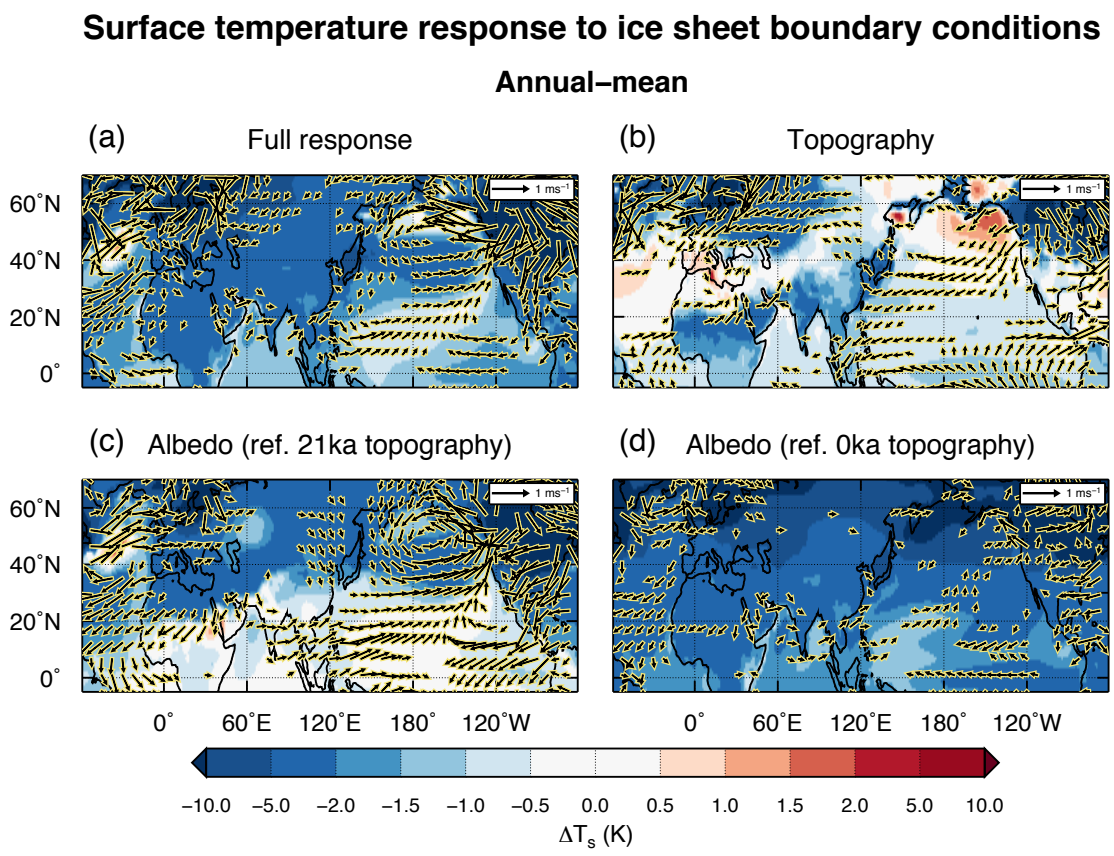

Fig. S7. Simulated surface temperature response to LGM ice sheets. As in fig. S6, but for sea-surface temperature (shading) and surface winds (vectors).

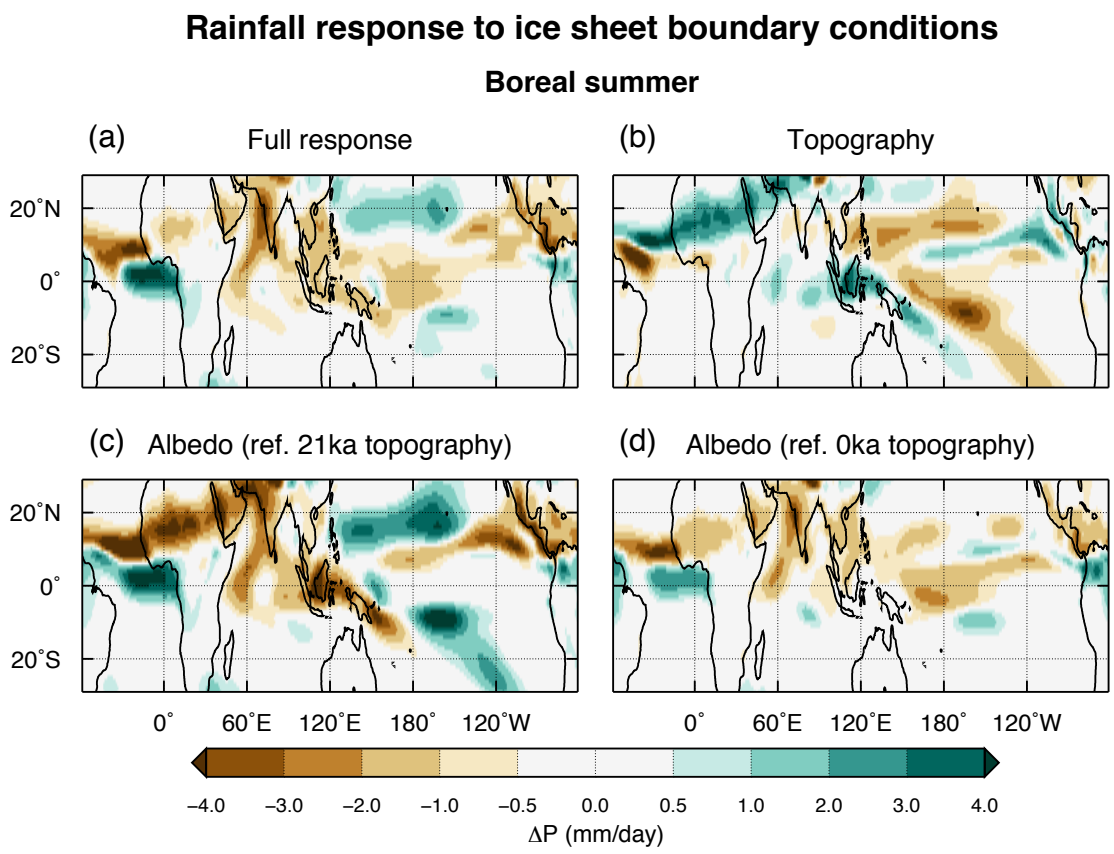

Fig. S8. Simulated boreal summer response to LGM ice sheets. As in fig. S6, but for July-August-September season.

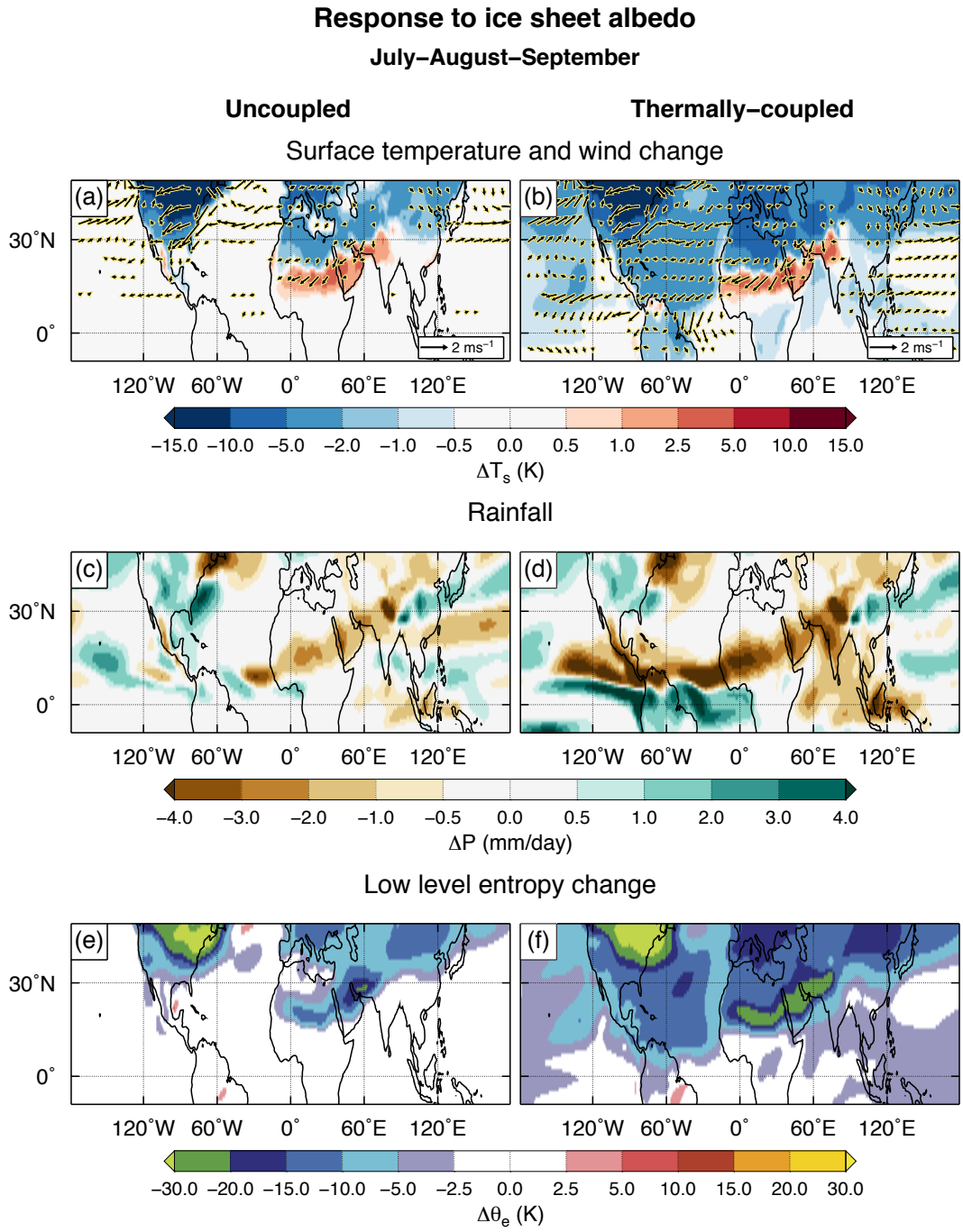

Fig. S9. Boreal summer response to ice sheet albedo as a function of ocean-atmosphere coupling. Changes in surface temperature (top), rainfall (middle), and low level entropy (bottom) during July-August-September (JAS) simulated by CESM1 in response to ice sheet albedo. Vectors indicate surface wind changes. Responses under varying degrees of ocean-atmosphere coupling are shown: CESM1 with fixed sea-surface temperatures (uncoupled) and with mixed-layer ocean model (thermally-coupled). The response with a fully interactive ocean model is not shown because it is identical to the thermally coupled case. Low level entropy is computed as the equivalent potential temperature on a terrain-following model level about 20 hPa above the surface as described in section 7.1.

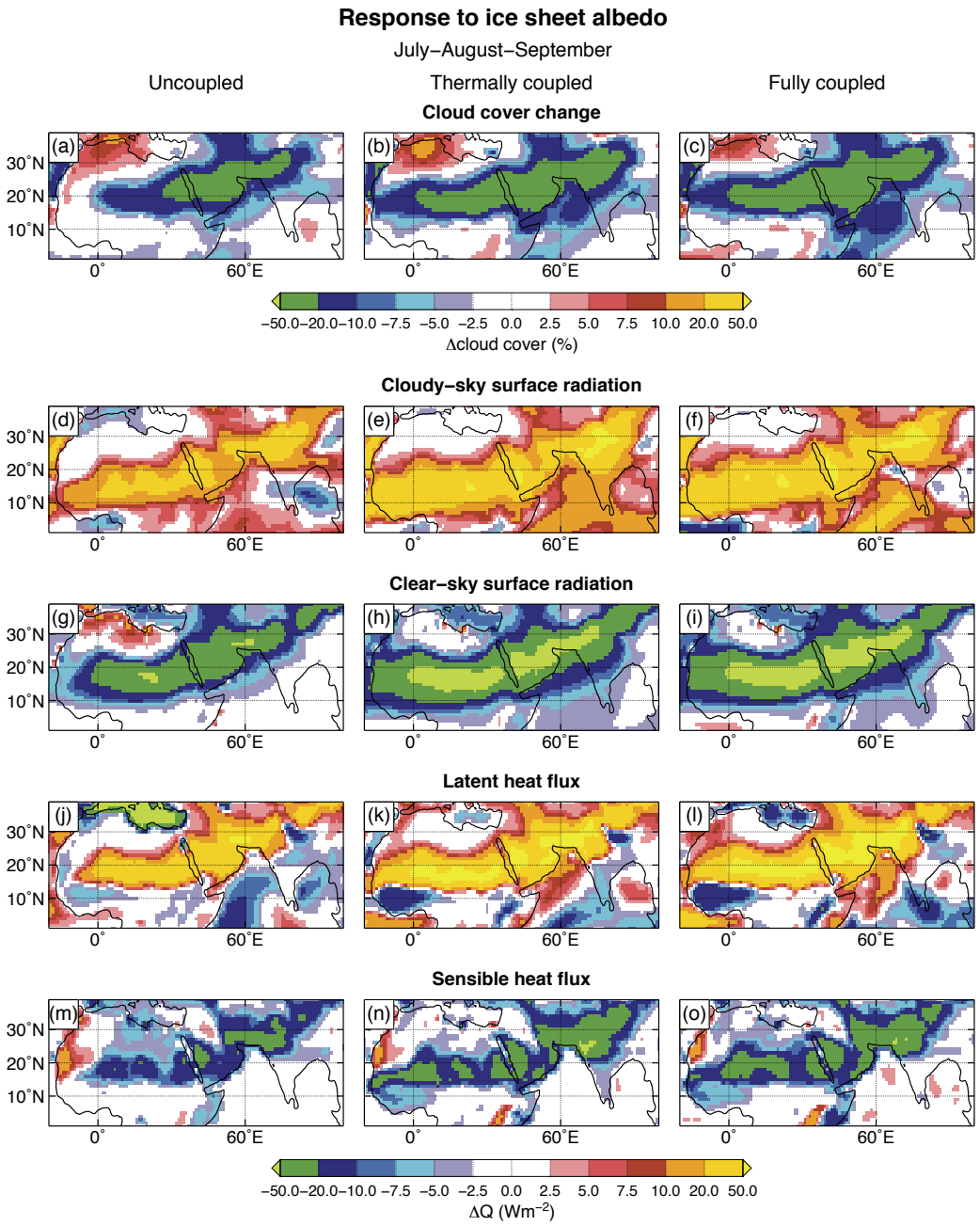

Fig. S10. Surface energy changes in response to ice sheet albedo as a function of ocean-atmosphere coupling. Changes in cloud cover, surface radiation in cloudy and clear sky, latent and sensible heat flux during July-August-September (JAS) simulated by CESM1 in response to ice sheet albedo. Positive energy flux changes indicate more energy entering the land or ocean surface. Responses under varying degrees of ocean-atmosphere coupling are shown, left to right: CESM1 with fixed sea-surface temperatures, with a mixed-layer ocean model, and with a fully interactive ocean model.

Table S1. Updates to the synthesis of LGM hydroclimate. List of sites added to the existing synthesis of LGM hydroclimate (*10*), with locations, hydroclimatic change category (W=wetter than present, NC=no change, D=drier than present, NR=not robust) and associated references. Updates to records already included in the synthesis are denoted with ^{u} in the category code.

Longitude	Latitude	Country/Region	Core/Site ID	Proxy	Category	Reference
41.60	11.10	Ethiopia/Djibouti	Lake Abhe	lake level	D^{u}	(*53*)
36.78	4.84	Southern Ethiopia	Lake Chew Bahir	K XRF counts	D	(*46*)
98.07	1.15	Northwest Sumatra	SO189-144KL	$\delta^{13}D_{wax}$, $\delta^{13}C_{wax}$	NC	(*102*)
118.38	2.87	Northeast Borneo	BJ8-03-91GGC	$\delta^{13}C_{CFA}$	NC	(*43*)
121.51	-2.73	Sulawesi (Indonesia)	Lake Towuti	$\delta^{13}C_{wax}$	D	(*3,39,40*)
119.36	-3.63	Mandar Bay	SO18515	$\delta^{13}C$, δD_{wax}	D	(*41*)
120.43	-8.53	Flores (Indonesia)	Liang Luar Cave	speleothem $\delta^{18}O$	D	(*42*)
120.92	-9.59	Sumba (Indonesia)	GeoB10069-3	$\delta^{13}C_{CFA}$	D	(*43*)
103.88	-6.33	Sumatra	MD98-2152	$\delta^{13}C_{wax}$	D	(*103*)
124.08	-17.33	Northern Australia	Ball Gown Cave	speleothem $\delta^{18}O$	D	(*44*)

Table S2. Compilation of SST proxies. List of sites and proxy sea-surface temperature data used in this study, including the core name, location, proxy type,whether cleaning for Mg/Ca analysis was reductive (if applicable), availability of ^{14}C chronology (in which case the age model was recalibrated onto the Marine13 curve), mean LGM temperature anomaly (across multiple proxies, if applicable; using BAYSPLINE with a 5σ prior for $U_{37}^{K'}$, the Gray 18 calibration for Mg/Cá-δ^{18}O, and BAYSPAR with a 10σ prior for TEX_{86}), 1σ uncertainty on the mean estimate, and reference in the literature. Time series data are denoted with ^{t}.Other data are timeslice data, consisting of mean LGM and late Holocene values only. Mg/Ca-δ^{18}O measurements were made on the species *Globigerinoides ruber* (white) with the exception of sites SK168/GC-1 and ERDC-092BX which contain measurements made on *Globigerinoides sacculifer*. *the chronology of MD77-194 is tied to that of SO42-74KL via use of 10 tiepoints.

Core	Lat.	Long.	W. Depth	Proxy	Red?	^{14}C?	ΔT LGM	1σ	Ref.
^{t}P178-15P	11.955	44.300	869	Mg/Ca-δ^{18}O, $U_{37}^{K'}$, TEX_{86}	X	X	-2.5	0.4	(*37*)
^{t}SO42-74KL	14.321	57.347	3212	Mg/Ca-δ^{18}O, $U_{37}^{K'}$, TEX_{86}		X	-2.6	0.7	(*104, 105*)
^{t}NIOP-C2 905PC	10.783	51.933	1567	$U_{37}^{K'}$, TEX_{86}		X	-2.0	0.2	(*104*)
^{t}SK237-GC04	10.978	74.999	1245	Mg/Ca-δ^{18}O		X	-2.9	0.1	(*106*)
^{t}MD77-194	10.467	75.233	1222	$U_{37}^{K'}$		*	-1.9	0.3	(*107*)
^{t}MD79-257	-20.240	36.200	1262	$U_{37}^{K'}$		X	-3.2	0.5	(*108*)
^{t}MD85-668	0.0167	46.033	4020	$U_{37}^{K'}$			-1.3	0.2	(*108*)
^{t}MD85-674	3.183	50.433	4875	$U_{37}^{K'}$			-1.9	0.4	(*108*)
^{t}MD90-963	5.067	73.883	2446	$U_{37}^{K'}$			-3.0	0.5	(*108*)
^{t}TY93929P	13.700	53.300	2490	$U_{37}^{K'}$			-2.2	0.5	(*108*)
SO28-11KL	5.390	60.252	3859	Mg/Ca-δ^{18}O	X		1.1	0.2	(*105*)
SO28-18KL	1.900	67.342	3035	Mg/Ca-δ^{18}O	X		-0.8	0.2	(*105*)
SO42-26KL	15.515	68.760	3776	Mg/Ca-δ^{18}O	X		-4.3	0.2	(*105*)
SO42-36KL	17.075	69.045	2055	Mg/Ca-δ^{18}O	X		-3.2	0.1	(*105*)
SO42-74KL	14.321	57.347	3212	Mg/Ca-δ^{18}O	X		-2.2	0.2	(*105*)
IOE-143KK	1.250	44.783	1522	Mg/Ca-δ^{18}O	X		-3.1	0.1	(*105*)
SO42-87KL	10.502	57.737	3773	Mg/Ca-δ^{18}O	X		-0.6	0.1	(*105*)
TN47-6GGC	17.382	58.795	3652	Mg/Ca-δ^{18}O	X		-9.4	0.2	(*105*)
MD79-254	-17.883	38.667	1934	$U_{37}^{K'}$			-1.7	0.3	(*107*)
MD79-256	-19.583	37.033	1222	$U_{37}^{K'}$			-1.7	0.3	(*107*)
MD77-180	18.467	89.850	1986	$U_{37}^{K'}$			-2.2	0.4	(*107*)
MD77-181	17.400	90.483	2271	$U_{37}^{K'}$			-3.5	0.4	(*107*)
MD77-176	14.517	93.133	1375	$U_{37}^{K'}$			-1.8	0.3	(*107*)
MD77-169	10.217	95.050	2360	$U_{37}^{K'}$			-2.5	0.4	(*107*)
MD76-131	15.883	72.567	1230	$U_{37}^{K'}$			-3.4	0.6	(*107*)
MD77-195	11.500	74.367	1426	$U_{37}^{K'}$			-2.2	0.3	(*107*)
MD77-191	7.502	76.717	1254	$U_{37}^{K'}$			-2.8	0.5	(*107*)
MD77-203	20.698	59.568	2442	$U_{37}^{K'}$			-3.6	0.8	(*107*)
MD77-202	19.222	60.682	2427	$U_{37}^{K'}$			-3.8	0.9	(*107*)
MD76-135	14.443	50.530	1895	$U_{37}^{K'}$			-2.3	0.5	(*107*)
TY93905P	10.700	51.930	1586	$U_{37}^{K'}$			-2.3	0.6	(*107*)
ODP723	18.070	57.610	816	$U_{37}^{K'}$			-2.7	0.5	(*107*)

Core	Lat.	Long.	W. Depth	Proxy	Red?	^{14}C?	ΔT LGM	1σ	Ref.
^{t}GeoB10029-4	-1.494	100.128	964	Mg/Ca-δ^{18}O		X	-2.7	0.1	(*109*)
^{t}GeoB10038-4	-5.938	103.246	1891	Mg/Ca-δ^{18}O, $U_{37}^{K'}$		X	-2.2	0.4	(*109*)
^{t}GeoB12615-4	-7.138	39.841	446	Mg/Ca-δ^{18}O		X	-2.6	0.1	(*110*)
^{t}GeoB3007-1	16.168	59.761	1920	$U_{37}^{K'}$			-3.1	0.5	(*111*)
^{t}GIK17940-2	20.117	117.383	1727	$U_{37}^{K'}$		X	-4.7	0.9	(*112*)
^{t}GIK17954-2	14.797	111.525	1520	$U_{37}^{K'}$			-5.2	0.9	(*112*)
^{t}GIK17961-2	8.507	112.332	1725	$U_{37}^{K'}$			-3.1	0.6	(*112*)
^{t}GIK17964-2	6.158	112.213	1556	$U_{37}^{K'}$			-3.0	0.6	(*112*)
^{t}SO93-126KL	19.972	90.033	1253	$U_{37}^{K'}$			-1.1	0.2	(*113*)
^{t}SO189-119KL	3.518	96.314	808	Mg/Ca-δ^{18}O		X	-3.0	0.1	(*114*)
^{t}SO189-39KL	-0.790	99.909	517	Mg/Ca-δ^{18}O		X	-3.4	0.1	(*114*)
^{t}SO90-136KL	23.122	66.497	568	$U_{37}^{K'}$			-5.0	0.9	(*115*)
Fr10/95-20	-24.750	111.830	841	$U_{37}^{K'}$			-1.8	0.3	(*116*)
Fr10/95-17	-22.130	113.500	1093	$U_{37}^{K'}$			-0.2	0.2	(*116*)
Fr2/96-27	-18.570	116.270	1023.5	$U_{37}^{K'}$			-0.04	0.2	(*116*)
SO90-93KL	23.588	64.216	1802	$U_{37}^{K'}$			-3.9	0.8	(*116*)
KH92-1-5cBX	3.530	141.870	2282	$U_{37}^{K'}$			-0.2	0.2	(*116*)
SO50-31 KL	18.750	115.880	3360	$U_{37}^{K'}$			-4.7	1.0	(*116*)
^{t}MD97-2138	1.420	146.235	1900	Mg/Ca-δ^{18}O, $U_{37}^{K'}$		X	-1.7	0.3	(*117*)
^{t}MD01-2378	-13.083	121.788	1783	Mg/Ca-δ^{18}O	X	X	-2.1	0.1	(*118*)
ODP1146	19.450	116.270	2092	Mg/Ca-δ^{18}O	X		-1.7	0.2	(*119*)
GIK17927-1	17.252	119.453	2804	Mg/Ca-δ^{18}O	X		-1.7	0.2	(*119*)
GIK17950-2	16.090	112.900	1868	Mg/Ca-δ^{18}O	X		-1.9	0.2	(*119*)
GIK17954-3	14.760	111.530	1517	Mg/Ca-δ^{18}O	X		-2.2	0.1	(*119*)
GIK17957-2	10.900	115.310	2195	Mg/Ca-δ^{18}O	X		0.1	0.1	(*119*)
GIK18459-3	-8.500	128.170	1744	Mg/Ca-δ^{18}O	X		-2.3	0.1	(*119*)
GIK18460-3	-8.790	128.640	1421	Mg/Ca-δ^{18}O	X		-3.1	0.1	(*119*)
GIK18473-2	-11.520	122.420	2468	Mg/Ca-δ^{18}O	X		-0.9	0.1	(*119*)
GIK18475-3	-11.300	121.700	1774	Mg/Ca-δ^{18}O	X		-2.1	0.1	(*119*)
GIK18476-2	-10.950	120.990	986	Mg/Ca-δ^{18}O	X		-2.3	0.1	(*119*)
GIK18477-4	-10.830	120.670	1478	Mg/Ca-δ^{18}O	X		-1.8	0.1	(*119*)
GIK18500-3	-14.980	120.700	1167	Mg/Ca-δ^{18}O	X		-2.9	0.1	(*119*)
GIK18506-2	-15.310	119.500	2410	Mg/Ca-δ^{18}O	X		-2.6	0.2	(*119*)
GIK18507-3	-13.850	120.000	2450	Mg/Ca-δ^{18}O	X		-2.1	0.2	(*119*)
MD98-2162	-4.690	117.900	1855	Mg/Ca-δ^{18}O			-3.1	0.1	(*119*)
^{t}GeoB10069-3	-9.010	120.015	1250	Mg/Ca-δ^{18}O	X	X	-1.5	0.1	(*120*)
^{t}MD98-2181	6.300	125.833	2114	Mg/Ca-δ^{18}O		X	-2.4	0.1	(*121*)
^{t}MD98-2176	-5.00	133.440	2382	Mg/Ca-δ^{18}O		X	-1.8	0.1	(*121*)
^{t}MD98-2170	-10.590	125.390	832	Mg/Ca-δ^{18}O		X	-2.5	0.1	(*121*)
^{t}SK168/GC-1	11.708	94.493	2064	Mg/Ca-δ^{18}O	X	X	-1.7	0.1	(*122*)
^{t}ERDC-092BX	-2.225	156.998	1598	Mg/Ca-δ^{18}O	X	X	-1.3	0.1	(*123*)
^{t}MD97-2146	20.117	117.384	1720	$U_{37}^{K'}$, TEX_{86}		X	-4.3	0.7	(*124, 125*)
^{t}MD97-2151	8.728	109.869	1598	$U_{37}^{K'}$, TEX_{86}		X	-3.3	0.6	(*126*)
^{t}GeoB12610-2	-4.817	39.424	399	Mg/Ca-δ^{18}O		X	-1.5	0.1	(*127*)

Table S3. Sea level simulations. Climate simulations performed with CESM1 under different combinations of sea level boundary conditions applied to the Maritime Continent domain (30°S–30°N, 90°E–160°E). ‡Duration of the equilibrated portion of the simulation used to compute climatologies. ⋆Time in years until equilibration. See section 4.2 for more details on the implementation of these boundary conditions.

	Sunda exposure	Sahul exposure	Passage bathymetry	Tidal mixing	Duration‡	Equilibration⋆
LGM_{SUNDA}	X				100	100
LGM_{SAHUL}		X			100	100
$LGM_{SUNDA+SAHUL}$	X	X			100	300
LGM_{SL}	X	X	X	X	400	500

Table S4. LGM and single-forcing simulations. Climate simulations performed with CESM1 under different combinations LGM boundary conditions. Crosses indicate the boundary conditions (columns) modified in each simulation (rows). All boundary conditions are applied globally unless specified. ⊛Greenhouse gas concentration values based PMIP3 experimental protocol, LGM values: CO_2= 280 ppm, CH_4= 760 ppb, NO_2= 270 ppb. ◇Based on a 120 m relative sea level drop with respect to PI values. ♮Bathymetry and land mask modified only over Maritime Continent (MC) region (30°S–30°N, 90°E–160°E). See section 4.2 for details on the implementation of these boundary conditions.‡Duration of the equilibrated portion of the simulation used to compute climatologies. ⋆Initialized from one of the equilibrated simulations as described in section 5. ⋆⋆Initialized from an existing equilibrated LGM simulation performed with a previous version of CESM1 as described in section 5.

	GHGs⊛	Orbit	Land mask & bathymetry◇	Topography	Albedo	Duration‡	Equilibration⋆
LGM_{GHG}	X					300	0⋆
LGM_{SL}			X♮			400	500
$LGM_{SL+GHG+ORB}$	X	X	X♮			400	300
LGM_{ICE}				X	X	400	700
LGM_{TOPO}				X		200	100
LGM_{ALB}					X	400	500
LGM_{ICE+SL}			X	X	X	500	0⋆
LGM	X	X	X	X	X	600	500⋆⋆